MDPI

Article

CFD Analysis of the Effect of Dimples and Cylinder Liner Honing Groove on the Tribological Characteristics of a Low Displacement Engine

Sofia Orjuela Abril *, Marlen Del Socorro Fonseca-Vigoya and Jhon Pabón-León

Programa de Administración de Empresas, Universidad Francisco de Paula Santander,
San José de Cúcuta 540001, Colombia; marlenfonseca@ufps.edu.co (M.D.S.F.-V.); jhonantuny@ufps.edu.co (J.P.-L.)
* Correspondence: sofiaorjuela@ufps.edu.co; Tel.: +57-7-5776655

Abstract: The contact between the piston rings and the cylinder liner is an interface with a strong influence on the tribological behavior and, therefore, directly affects the useful life of the engine components and fuel consumption. Due to this importance, the present investigation carried out an analysis of the effects of dimples and the honing groove in the cylinder liner on the tribological characteristics. A tribological model was developed to study the friction forces, minimum film thickness, and friction coefficient for the present investigation. Similarly, a computational fluid dynamics model was built to determine the dynamic movement of the piston. The validation of the numerical model showed a close similarity with the real behavior of the engine, obtaining an average relative error of 14%. The analysis of the results showed that a 3% increase in dimples' density leads to a 3.79% increase in the minimum lubricant film and a 2.76% decrease in friction force. Additionally, it was shown that doubling the radius and depth of the dimple produces an increase of 3.86% and 1.91% in the thickness of the lubrication film. The most suitable distribution of the dimples on the surface of the cylinder liner corresponds to a square array. In general, the application of dimples and honing grooves in the cylinder liner are promising alternatives to reduce energy losses and minimize wear of engine components.

Keywords: engine piston; surface dimples; honing groove; cylinder liner; coefficient friction; tribology

1. Introduction

One of the main objectives for designing components in internal combustion engines (ICE) is to avoid the high energy losses associated with friction phenomena and maximize the durability of components and conjunctions exposed to surface contacts. This is necessary for the production of more efficient ICE, which implies a reduction in fuel consumption levels. In this way, compliance with increasingly stringent global regulations and standards for the control of emissions that are harmful to the environment is facilitated [1,2]. Studies indicate that, inside internal combustion engines, losses associated with friction phenomena by components in surface contact are responsible for 20% of total energy losses. The main sources of these friction losses correspond to the contact between the piston ring–cylinder liner and piston skirt–cylinder liner, which are responsible for 40% of this type of energy loss [3,4].

The function of the piston rings is to supply a tight seal between the space between the cylinder liner and the piston skirt. Additionally, such fitment allows the control and distribution of the lubrication oil, as well as the transfer of heat from the piston. However, this causes a significant amount of friction loss due to simultaneous sealing and sliding. Therefore, tribological performance improvement is one of the main strategies for achieving a fuel economy benefit. The studies carried out show that the friction losses due to the contact between the piston rings and the cylinder liner are responsible for 4–15% of the total fuel consumption of the engine [5]. As internal combustion engines continue to play

leading roles in the coming decades, it is necessary to search for strategies to reduce energy losses in the piston–cylinder liner assembly through friction reduction [6].

The analysis of tribological behavior in the piston assembly requires the analysis of multiple variables, such as surface topography, transient lubrication, ring dynamics, exhaust flow rate, etc. Additionally, each variable presents interactions with each other, becoming a complex analysis. Due to the above, research focused on tribological characteristics is generally focused on evaluating a single variable. Among the first investigations is the study by Furuhama and Sumi [7], which investigated the lining of compression rings. Ma et al. [8] built a model to analyze the transport of lubricating oil. The results indicated that the cylinder liner surface and ring movement significantly influence the tribological behavior of the piston. Akalin and Newaz [9] investigated the conditions of the mixed compression ring lubrication regime using the Reynolds equations. Jeng [10] used the Reynolds lubrication theory to analyze the lubrication conditions at the compression ring contact surface. Furuhama and Sasaki [11] evaluated the influence of friction forces on the piston for small engines. Tian [12] implemented an experimental and numerical methodology to study piston ring dynamics. The investigation took into account torsion, changes in lubricant film thickness, and ring liner wear.

In recent years, research has been carried out focused on improving the efficiency of internal combustion engines. Among the studies carried out is the research developed by Morris et al. [13], which focused on the optimization of the piston compression ring in high-performance racing engines. Bewsher et al. [14] studied the limit friction prediction of the piston ring assembly and cylinder liner by atomic force microscopic (AFM) to improve engine efficiency. Usman and Park [15] investigated the effect of surface texturing in reducing piston friction losses. Another area of research for reducing friction losses is focused on the cylinder liner. Smith et al. [16] simultaneously tested lubricant coating and surface texture for friction loss reduction. Li et al. [17] investigated the effect of laser finishing on the cylinder liner. The results indicate an improvement in tribological performance.

Another alternative to achieve an improvement in the tribological characteristics is the implementation of textured surfaces. Senatore et al. [18] investigated the change in the coefficient of friction and wear in a bronze coating with different surface texturing conditions. The results indicated that the application of textures causes better tribological properties of the coating. Shum and Zhou [19] reported that laser surface texturing improves wear resistance in diamond-like carbon coatings. Wang et al. [20] carried out experimental tests on the effect of dimples on the surface of brass discs. The results indicated that the presence of dimples favors the reduction in friction. Kligerman et al. [21] developed an analytical model to evaluate the power of partial laser surface texturing (LST) in reducing friction between the cylinder liner and the piston ring. Spencer et al. [22] studied the texturing of cross-hatch grooves on the cylinder liner surface to minimize oil consumption, reduce friction, and prevent engine component wear. Lu and Wood [23] reported that partial texturing allows achieving a reduction in friction conditions of 34.5% in cutting tools, 18% in plain bearings, 65% in seals, and 82% in piston rings. Etsion [24] mentioned that laser surface texturing can be successfully applied to cylinder liners and piston rings, which can result in a reduction of up to 4.5% in engine fuel consumption.

The ring–cylinder liner surface contact is considered one of the four main surface contacts in the engine [25]. The other three surfaces correspond to the contact between the piston pin and connecting rod, main crankshaft bearings, and valve train. Several investigations have studied the surface textures of the ring and cylinder liner coating to reduce friction losses. Hu et al. [26] showed that the storage of lubrication oil in the scratched textures allows for improving the tribological performance of the piston rings. Vladescu et al. [27] studied the influence of surface texture on oil thickness under complete lubrication conditions. Pawlus et al. [28] studied the honing parameters that influence surface topography. Jeng [29] indicated that flat surfaces cause less wear and friction. Vladescu et al. [30] investigated the behavior of lubricating oil with parallel and transverse grooves on the piston ring–liner contact surface.

The research presents as a novelty a detailed analysis of the influence of the geometric parameters of two different types of cylinder liner textures—namely, dimples and honing grooves. As the surface texture affects the tribological characteristics, the present investigation aims to evaluate the effect of dimples and honing grooves on the cylinder liner on the tribological behavior. Texture parameters such as depth, density, and distribution were investigated.

2. Tribological Model

2.1. Hydrodynamic Pressure

The hydrodynamic pressure between the piston ring and the cylinder liner was determined by the Reynolds equation proposed by Guo et al. [31], which is indicated below.

$$\frac{\partial}{\partial x}\left(\frac{\partial P}{\partial x}\frac{\rho h^3}{\mu}\phi_x\right) + \frac{\partial}{\partial y}\left(\frac{\partial P}{\partial y}\frac{\rho h^3}{\mu}\phi_y\right) = 6v_p\phi_c\frac{\partial h}{\partial x} + 6v_p\sigma\frac{\partial \phi_s}{\partial x} + 12\phi_c\frac{\partial h}{\partial t} \tag{1}$$

where ρ and μ are the density and dynamic viscosity of the lubricating oil, v_p is the piston velocity, h is the thickness of the lubrication film, P is the mean hydrodynamic pressure between the piston and the cylinder liner, ϕ_s is the shear flow factor, ϕ_x and ϕ_y are the pressure-flow factors, ϕ_c is a contact factor, and σ is the composite roughness, respectively. The pressure-flow factors ϕ_x and ϕ_y were determined from Equation (2) [32].

$$\phi_x = \phi_y = 1 - 0.9e^{-0.56\lambda} \tag{2}$$

where λ is the ratio of the thickness of the lubrication film over surface roughness ($\lambda = h/\sigma$).

To calculate the density of the lubricating oil, the model proposed by Dowson and Higginson [33] was used, as shown in Equation (3).

$$\rho = \rho_{atm}\left[\frac{6 \times 10^{-10}(P - P_{atm})}{1 + 1.7 \times 10^{-9}(P - P_{atm})} + 1\right][1 - \varrho(T - T_{atm})] \tag{3}$$

where ϱ and T are the thermal coefficient of expansion and the temperature of the lubricating oil. The subscript atm refers to environmental conditions.

The dynamic viscosity of the lubricating oil was determined using the equation proposed by Houpert [34], as indicated in Equation (4).

$$\mu = \mu_{atm} \times \exp\left(\left[\left\{1 + \frac{P - P_{atm}}{c_p}\right\}^z\left\{\frac{T - 138}{T_o - 138}\right\}^{-s_o} - 1\right] \times \ln\left[\frac{\mu_{atm}}{\mu_\infty}\right]\right) \tag{4}$$

where z and s_o are the lubricant piezo-viscosity and thermo-viscosity indices, calculated from Equations (5) and (6).

$$z = \frac{\propto_o c_p}{\ln\left[\frac{\mu_{atm}}{\mu_\infty}\right]} \tag{5}$$

$$s_o = \frac{\beta_s(T_o - 138)}{\ln\left[\frac{\mu_{atm}}{\mu_\infty}\right]} \tag{6}$$

where $\propto_o$ is the atmospheric piezo-viscosity coefficient, β_s is the thermo-viscosity coefficient, and $c_p = 1.98 \times 10^8$ Pa and $\mu_\infty = 6.31 \times 10^{-5}$ Pa·s are model constants, respectively.

As the cylinder liner surface texture distribution changes in relation to piston movement, the lubricating oil film thickness is determined as a function of position (x, y) and time (t), as is shown in Equation (7).

$$h(x, y, t) = h_m + h_s + h_p + h_h \tag{7}$$

where h_m is the minimum film thickness; h_s is the profile of the ring piston; h_p and h_h are the variation in the thickness of the lubricating oil film due to the dimples on the cylinder liner and the honing grooves. To determine h_s, Equation (8) was used [35].

$$h_s = \frac{4\delta_o}{b^2} x^2 \tag{8}$$

where δ_o is the crown height and b is the piston ring axial width, respectively. Equation (9) was used to calculate the thickness h_p [36].

$$h_p = \left[\left(\frac{r_d^2 + h_d^2}{2h_d} \right)^2 - \chi^2 - \gamma^2 \right]^{1/2} - \frac{r_d^2 - h_d^2}{2h_d} \tag{9}$$

where r_d is the dimple radius, h_d is the maximum depth of a dimple, χ and γ are the local cartesian coordinates for a single dimple cell. Equation (10) was used to generate the honing groove texture on the cylinder liner surface [37].

$$h_h = \cos(2\pi[x + \kappa y]) \times 10^{-\omega[x+\kappa y]^2} \tag{10}$$

where κ is the honing angle parameter, and ω is the honing width parameter, respectively.

2.2. Friction Model

The interaction between the piston ring and the cylinder liner results in a viscous frictional force (f_v) caused by the lubricating oil film, and a boundary frictional force (f_b) caused by the interaction of surface asperities protruding from the oil film. Therefore, the total frictional force (f_T) at the piston ring and cylinder liner contact was determined from Equation (11).

$$f_T = f_v + f_b \tag{11}$$

The viscous friction force was calculated by Equation (12).

$$f_v = v_{ss}(A - A_c) \tag{12}$$

where v_{ss} is the viscous shear stress of the lubricating oil, A is the apparent contact area and A_c is the real contact area between the piston ring and cylinder liner, respectively. The variable A_c was calculated using Equation (13).

$$A_c = AF_2(\pi\xi\varphi\sigma)^2 \tag{13}$$

where ξ is the asperity distribution per unit contact area and φ is the average asperity tip radius of curvature. F_2 is a statistical function of the Stribeck lubricant film ratio, determined by Equation (14).

$$F_2 = \left\{ \begin{array}{cc} -0.0018\lambda^5 + 0.0281\lambda^4 - 0.1728\lambda^3 + 0.5258\lambda^2 - 0.8043\lambda + 0.5003 & \lambda \leq 2.295 \\ 0 & \lambda > 2.295 \end{array} \right\} \tag{14}$$

where λ is the Stribeck lubricant film ratio defined previously.

The viscous shear stress of the lubricating oil depends on the hydrodynamic pressure (P), the viscosity of the lubricant (η), and the film thickness (h) [38], as indicated in Equation (15).

$$v_{ss} = \left| \vec{v}_p \frac{\eta}{h} \pm \vec{\nabla}P \frac{h}{2} \right| \tag{15}$$

The boundary friction force was determined by Equation (16).

$$f_b = \varsigma W_a + \tau_o A_c \tag{16}$$

where ς is the coefficient of asperity shear strength ($\varsigma = 0.17$), and τ_o is the limiting Eyring shear stress ($\tau_o = 2 \times 10^6$ Pa) [39]. W_a is the asperity contact load, which was determined as shown in Equation (17) [40].

$$W_a = \frac{16\sqrt{2}\pi}{15} A F_{5/2} E'(\xi\varphi\sigma)^2 \left(\frac{\sigma}{\varphi}\right)^{1/2} \tag{17}$$

where E' is the effective Young's modulus of elasticity of the contact pair, calculated from Equation (18).

$$\frac{1}{E'} = \frac{1 - v_c^2}{E_c} + \frac{1 - v_p^2}{E_p} \tag{18}$$

where E is the modulus of elasticity and v is the Poisson's ratio, respectively. The subscripts p and c indicate the piston ring and cylinder liner.

The oil film ratio statistical function ($F_{5/2}$) is approximated by a polynomial, as shown in Equation (19) [41].

$$F_{5/2} = \left\{ \begin{array}{ll} -0.0046\lambda^5 + 0.0574\lambda^4 - 0.2958\lambda^3 + 0.7844\lambda^2 - 1.0776\lambda + 0.6167 & \lambda \leq 2.224 \\ 0 & \lambda > 2.224 \end{array} \right\} \tag{19}$$

3. Materials and Methods

To consider realistic loading conditions in the tribological model, a CFD model was used to describe the dynamic behavior of the piston. The development of the numerical simulations was carried out using the free software OpenFOAM®. For the CFD model, the characteristics of a four-stroke diesel engine were taken as a basis. The basic technical characteristics of the engine are indicated in Table 1.

Table 1. Characteristics of the reference engine.

Model	4JJ1-ISUZU
Engine type	4 cylinders
Bore × stroke	95.4 × 104.9 mm
Compression ratio	17.5:1
Injection type	Direct injection
Volume	2.999 L
Cycle	4 Strokes

The properties of the lubricating oil are based on the SAE 10W40 lubricant, whose physicochemical characteristics are shown in Table 2.

Table 2. Physicochemical properties of lubricating oil.

Properties	Unit	SAE 10W40
Kinematic viscosity (40 °C)	m^2/s	91.057×10^{-6}
Density (40 °C)	kg/m^3	866
Flash point	°C	230
Dynamic viscosity (40 °C)	m^2/s	105.10×10^{-6}
Pressure–viscosity coefficient	m^2/N	1×10^{-8}

The geometric CAD used for the numerical simulations is formed by the cylinder liner, connecting rod, crankshaft, and piston, as indicated in Figure 1. The geometric characteristics of the engine CAD are described in Table 3.
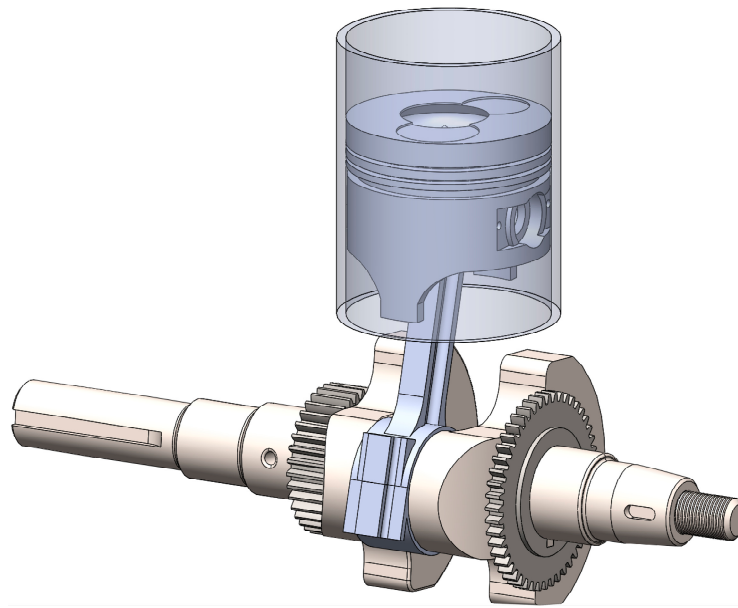
Figure 1. Test engine piston geometry.

Table 3. Geometric characteristics of the engine.

Parameter	Value	Unit
Piston area	4778.36	mm^2
Piston mass	0.305	kg
Length of piston skirt	48	mm
Length of connecting rod	106	mm
Crankshaft radius	48	mm
Piston radius	39	mm

The geometric characteristics of the engine CAD are described in Table 3.

The computational domain is the boundary by the surface of the cylinder liner, the piston skirt, and the rings' surface. Additionally, the domain involves the cylinder and the crankcase to represent all the movement of the piston during the stroke. Navier–Stokes's equations govern the behavior of the numerical simulation. The convergence of the numerical simulations was determined when the residuals reached a value of 10^{-4} in the dissipation rate, 10^{-4} in the turbulent kinetic energy, and 10^{-7} in the energy [42]. The initial data supplied in the numerical simulation comprise the engine's rotational speed, the crank angle range of operation, the intake pressure, the cylinder wall temperature, and the inlet temperature during the closing of the intake valve. The characteristics of the contours used in the simulations are shown in Table 4.

Table 4. Numerical simulation contours.

Region	Type
Cylinder wall Exhaust port Combustion chamber Intake port	Stationary wall
Intake valve Exhaust valve Piston	Moving wall
Air inlet	Inlet
Exhaust outlet	Outlet

The equations that govern the numerical simulation of the engine, involving the conservation of mass, conservation of momentum, conservation of energy, and turbulence model, are described below.

$$\frac{\partial(\rho u_i)}{\partial x_i} + \frac{\partial(\rho)}{\partial t} = 0 \tag{20}$$

$$\frac{\partial(\rho u_i u_j)}{\partial x_j} + \frac{\partial(\rho u_i)}{\partial t} = -\frac{\partial P}{\partial x_i} + \frac{\partial \tau_{ij}}{\partial x_j} + \rho g \tag{21}$$

$$\frac{\partial(\rho u_j h_o)}{\partial x_j} + \frac{\partial(\rho h_o)}{\partial t} = \frac{\partial P}{\partial t} + \frac{\partial(u_i \tau_{ij})}{\partial x_j} + \frac{\partial}{\partial x_j}\left(\psi \frac{\partial T}{\partial x_j}\right) + \rho q_r \tag{22}$$

$$\frac{\partial}{\partial x_j}(\rho u_j m_l) + \frac{\partial}{\partial t}(\rho m_l) = \frac{\partial}{\partial x_j}\left(\Gamma_l \frac{\partial m_l}{\partial x_j}\right) + R_l \tag{23}$$

where ρ is the fluid density, u is the fluid velocity, h_o is the stagnation enthalpy, t is the time, P is the pressure, g is the gravitational acceleration, τ_{ij} is the viscous shear stress tensor, q_r is the radiant heat, ψ is the heat conduction coefficient, R_l is the production rate caused by chemical reactions, and m_l is the mass fraction, respectively.

The geometric CAD mesh was generated using SALOME software. The type of 3D mesh used in the present investigation was the hexahedral mesh, with a maximum size of 1 mm. Figure 2 shows the piston's meshing and the engine's connecting rod.
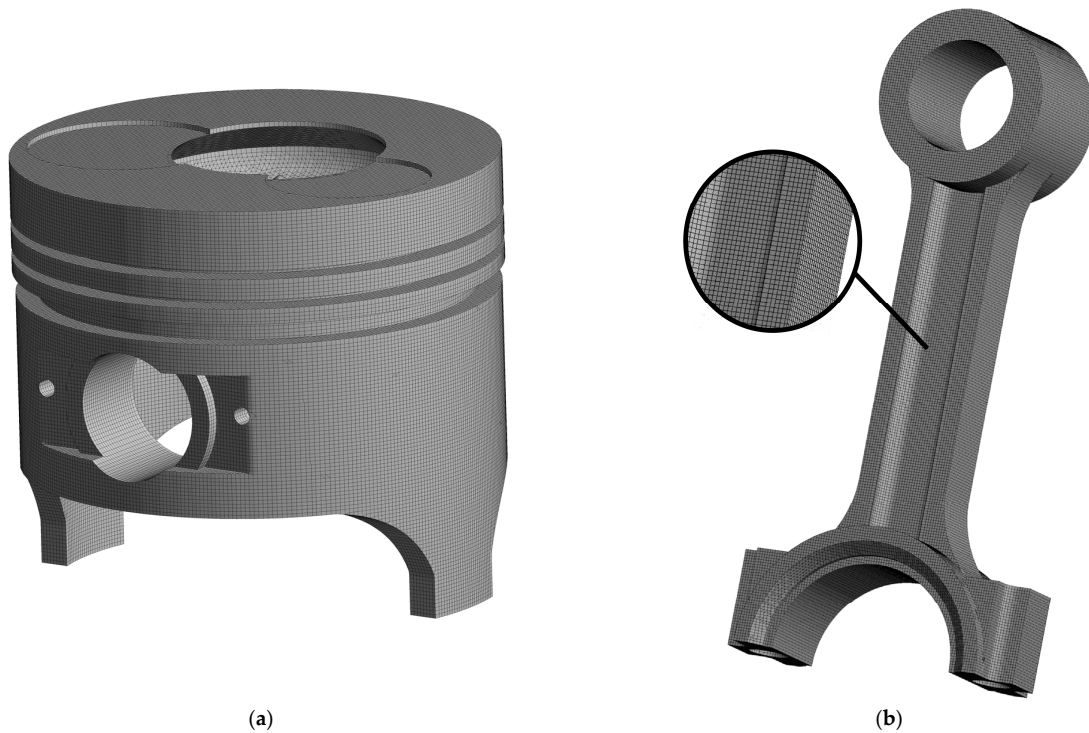

(**a**)   (**b**)

Figure 2. Geometric CAD meshing: (**a**) piston and (**b**) connecting rod.

To guarantee the reliability of the mesh, a mesh independence analysis was performed with different numbers of elements. The results obtained are shown in Figure 3.

Figure 3 shows the friction force throughout the combustion cycle for different numbers of mesh elements. The results show that from a number of elements of 2.4×10^6, it is possible to achieve stabilization in the predictions of the simulation. Indeed, the variation was less than 1.5%, compared with the previous number of elements (1.8×10^6). Therefore, a mesh with a number of elements of 2.4×10^6 was selected for the subsequent simulations.
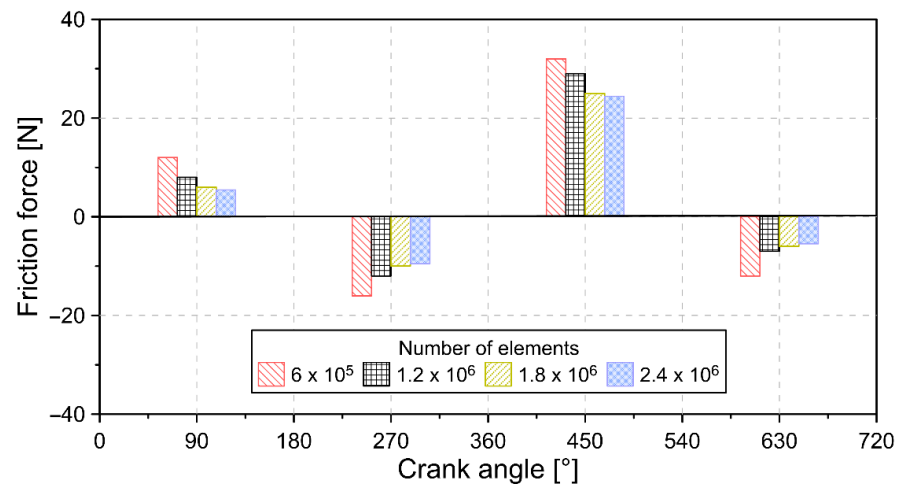
Figure 3. Mesh independence analysis.

From the results of the numerical simulation, the pressure and temperature curves were obtained throughout the combustion cycle and were used as input data in the tribological model. The data obtained for pressure and temperature are shown in Figure 4.
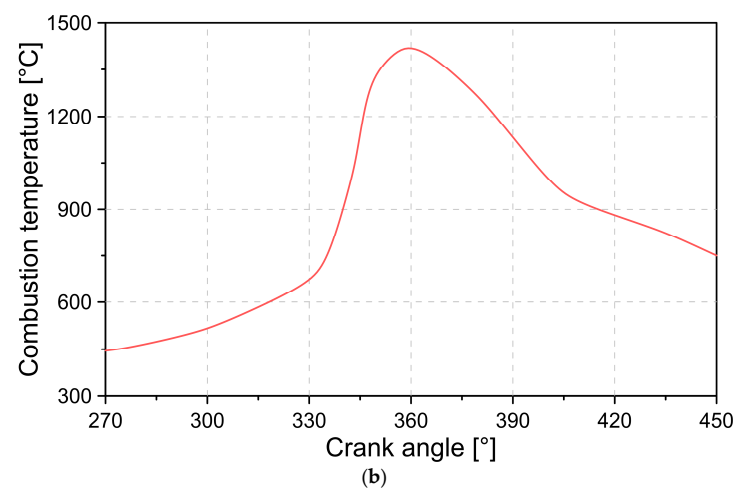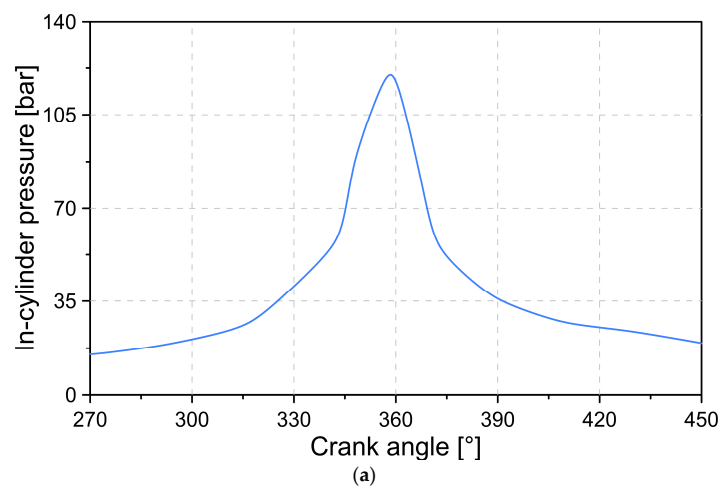

(a)

(b)

Figure 4. Numerical simulation predictions: (**a**) combustion pressure and (**b**) temperature.

To validate the constructed model, experimental tests were carried out to compare the results with the numerical model. Figure 5 shows the experimental engine test bench.
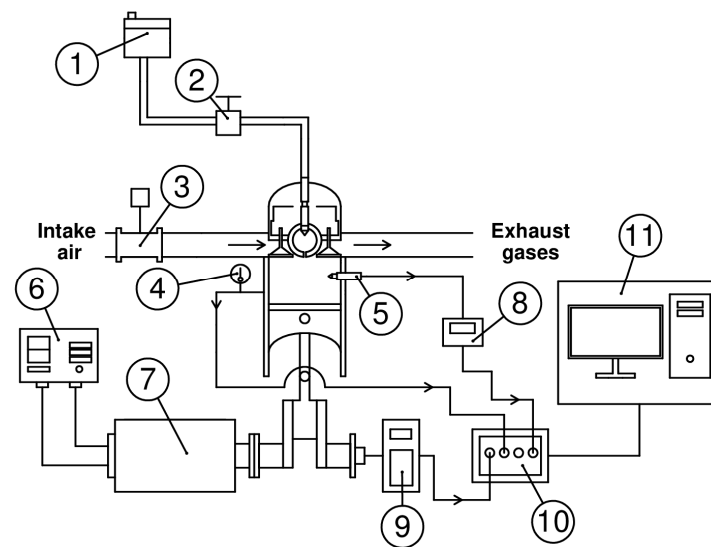
Figure 5. Experimental test bench: 1. fuel tank, 2. fuel control valve, 3. airflow indicator, 4. thermocouple, 5. pressure transductor, 6. load bank control, 7. electrical load bank, 8. charge amplifier, 9. crank angle encoder, 10. data acquisition system, 11. Computer.

The test bench engine is connected to a resistive load bank, which is used to control the rotational speed and torque. The measurement of the pressure of the combustion chamber was carried out by means of a piezoelectric sensor (KISTLER type 7063-A, KISTLER, Barcelona, Spain). A crankshaft angle sensor (Beck Arnley 180-0420, Beck/Arnley, Tennessee, EE.UU.) was used to measure the rotational speed. The mass flow of fuel was determined using a gravimetric meter (OHAUS PA313, OHAUS, Cundinamarca, Colombia). K-type thermocouples measured the temperature inside the combustion chamber. A hot-wire type sensor (BOSCH 22,680 7J600, BOSCH, Cundinamarca, Colombia) was used to measure the mass flow of the intake air. The characteristics of the measuring instruments are shown in Table 5. The methodology used for the development of the research is shown in Figure 6.

Table 5. Technical characteristics of measuring instruments.

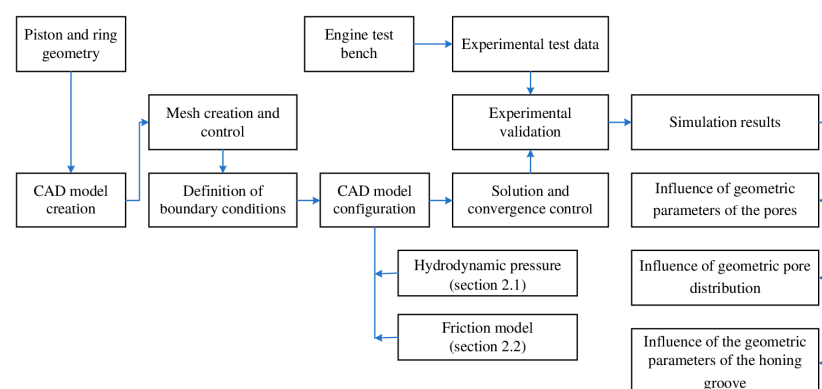| Model	Instrument	Parameter	Range	Uncertainty [%]
KISTLER type 7063-A	Piezoelectric transducer	Cylinder pressure	0–250 bar	±0.5%
Beck Arnley 180-0420	Crankshaft angle	Angle	5–9999 RPM	±1.0%
BOSCH 22,680 7J600	Intake air flow	Air flow	0–125 g/s	±0.15%
OHAUS PA313	Gravimetric meter	Fuel flow	0–310 g	±0.5%
Type K	Thermocouple	Temperature	−200–1370 °C	±0.1%

Figure 6. Research methodology using CFD.

From the geometric characteristics of the engine, the construction of the CAD of the piston–connecting rod–crankshaft assembly for the CFD model was carried out. The configuration of the CFD model is complemented by the tribological model described in Section 2. To define the model's boundary conditions, experimental data on pressure, flow, and temperature conditions in the combustion chamber were collected through the development of experimental tests. The tests were carried out at a rotation speed of 1800 rpm and a torque of 400 Nm. The initial condition of lubrication oil distribution was defined with a thickness of 5 um. This condition refers to the initial coating film on the cylinder liner. Additionally, the contact area between the piston ring face and the cylinder liner was established with a distribution of 90% air and 10% lubricating oil.

For the development of the study, two types of geometric patterns are evaluated on the cylinder liner. The structure of the patterns studied is shown in Figure 7.
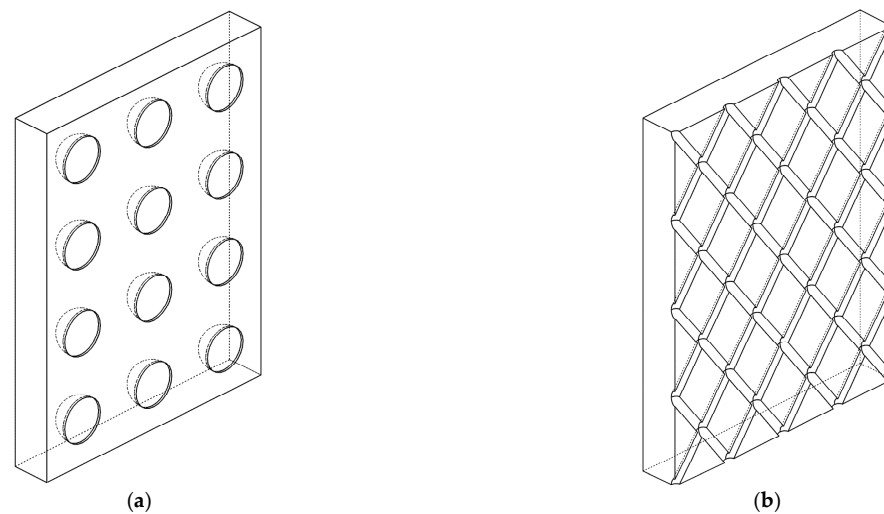

(a)　　　　　　　　　　　　　　　　　　　　　　　　　　(b)

Figure 7. Geometric patterns on the cylinder liner: (**a**) spherical dimples and (**b**) honing grooves.

In the case of spherical dimple patterns, two types of dimple density (3% and 6%) and two dimple depths (2 μm, 3 μm, and 4 μm) were analyzed, respectively. For the honing grooves, the effect of three depths (1 μm, 2 μm, and 3 μm) and a density range between 0.5 and 2.5 mm^{-2} were analyzed.

The validation of the numerical model was carried out by comparing the friction force produced in the piston throughout the combustion cycle, obtained through numerical simulation and experimental tests. The friction force was calculated by means of the transverse force on the cylinder liner. For this, a strain gauge sensor was used to calculate the deformation and stress in the cylinder liner. The characteristics of the sensor are indicated in Table 6.

Table 6. Strain gauge sensor.

Parameter	Value	Unit
Gauge resistance	120	Ω
Overall length × Grid width	6.30 × 4.55	mm
Gage length	2.54	mm
Overall width	4.55	mm
Maximum operating temperature	1150	°C

Since the increase in temperature inside the cylinder produces thermal deformation, a filtering process was carried out. The foregoing was carried out by restoring the signal after reaching stability in the temperature conditions and considering that the engine cylinder has a thermal coefficient of expansion of 24 μstrain/°C [43]. In this way, it is guaranteed that

the measurement made is caused by the mechanical deformation of the cylinder. Finally, the friction force was calculated using Equations (24) and (25) [44].

$$\frac{V_1}{V_2} = -\frac{\varepsilon \cdot G_f}{4 + 2\varepsilon \cdot G_f} \tag{24}$$

$$F_c = \varepsilon \cdot E_c \cdot A_s \tag{25}$$

where A_s is the area of the strain gauge sensor, V is the voltage, ε is the longitudinal unit strain, E_c is Young's modulus of the cylinder liner, F_c is the experimental friction force, and G_f is the calibration factor $\left(G_f = 2\right)$.

To prepare the inner surface of the cylinder liner, a plateau honing process was first performed before surface texture processing. Subsequently, machining was applied using a computer numerical control (CNC) machine to make the honing groove texture (Figure 7), with a depth of 3μm and an inclination angle of 45°, respectively. The experimental setup for friction force signal processing is indicated in Figure 8.
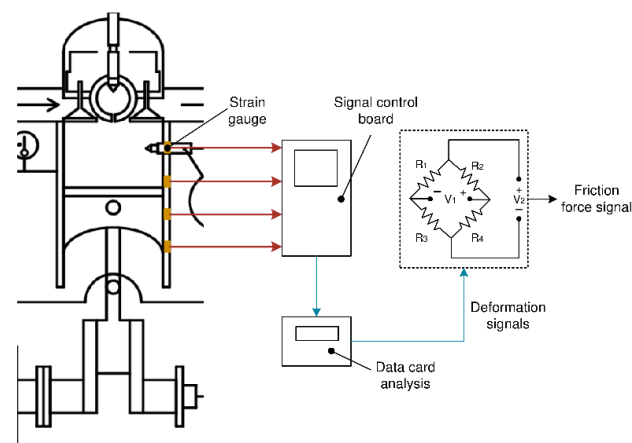

Figure 8. Measurement process of the friction force signal.

4. Results and Discussion

4.1. Validation of the Numerical Model

Figure 9 shows the comparison of the friction force obtained through the numerical simulation and the experimental tests.
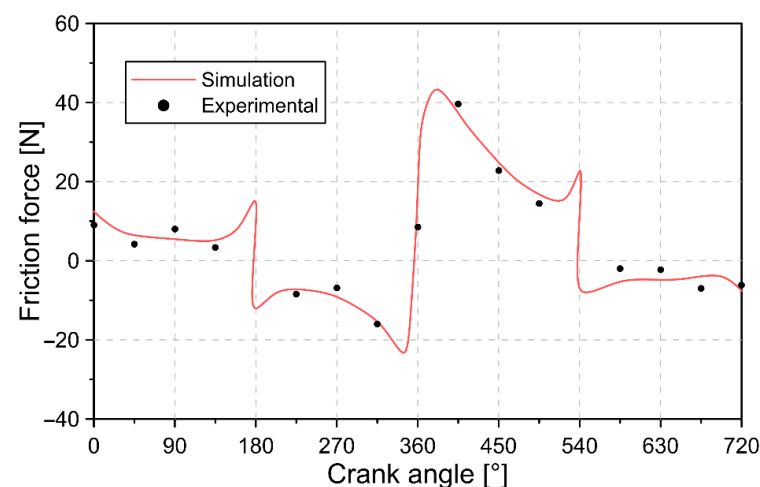

Figure 9. Comparison of the friction force between numerical and experimental results.

From the results described in Figure 9, it is evident that the curve obtained by numerical simulation represents similar trends, compared with the experimental results. On average, the relative error of the prediction of the numerical simulations was 14%, respectively. However, the maximum relative error achieved for the test conditions was 30%. This deviation can be attributed to multiple factors, such as variations in each combustion cycle, irregularity in the lubricant film due to the engine's splash mechanism, sudden changes in pressure, and alterations in the properties of the lubricant. Despite the above, the trends and estimates of the numerical model maintain a high concordance, compared with the experimental data, since the deviations obtained are similar to the results described in the literature [45,46].

From the behavior described in Figure 9, it was revealed that the greatest friction force occurs for a crank angle close to 360°, which coincides with the start of the cylinder expansion stage. During this stage, the pressure inside the chamber increases significantly, and the normal forces between the piston ring and the cylinder liner increase. Therefore, the frictional force during this part of the combustion cycle is greater than that seen at other crank angles. The results obtained are in agreement with reports in the literature [9].

4.2. Influence of Geometric Parameters on the Dimples Density

To analyze the effect of the dimples in the cylinder liner on the tribological characteristics of the engine, an analysis of the trends of the minimum film thickness and the friction force throughout the combustion cycle was carried out for two levels of dimple densities of 3% and 6%, in a flooded lubrication condition. Figure 10 shows the minimum oil film thickness change for 3% and 6% dimple density under a flooded lubrication condition.
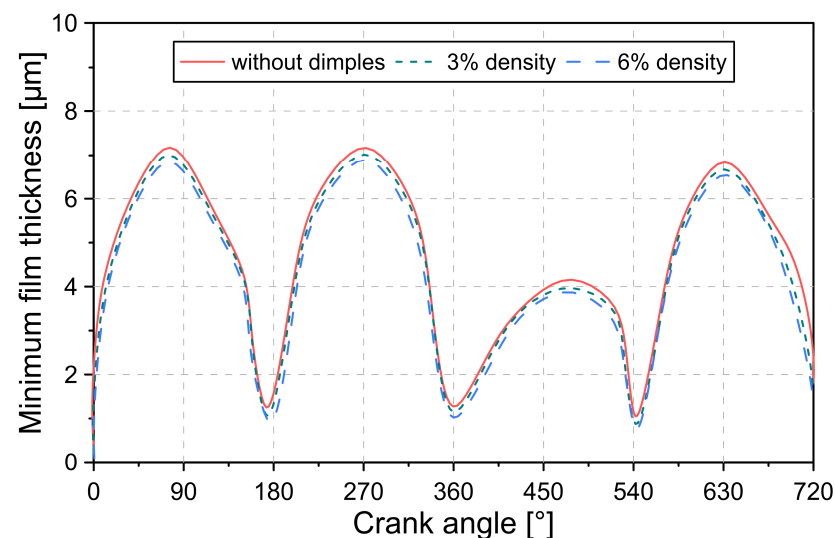

Figure 10. Minimum film thickness for different dimple densities in flooded lubrication.

The results obtained in Figure 10 indicate that the increase in dimple density produces a decrease in the thickness of the lubrication film. To demonstrate the effect of the dimples on the surface of the cylinder liner, an analysis of the ratio between the minimum thickness of the lubrication film (h_m) and the clearance between the cylinder liner and the piston (l_{cl}), indicated in Equation (26), was performed.

$$\xi_s = \frac{h_m}{l_{cl}} \tag{26}$$

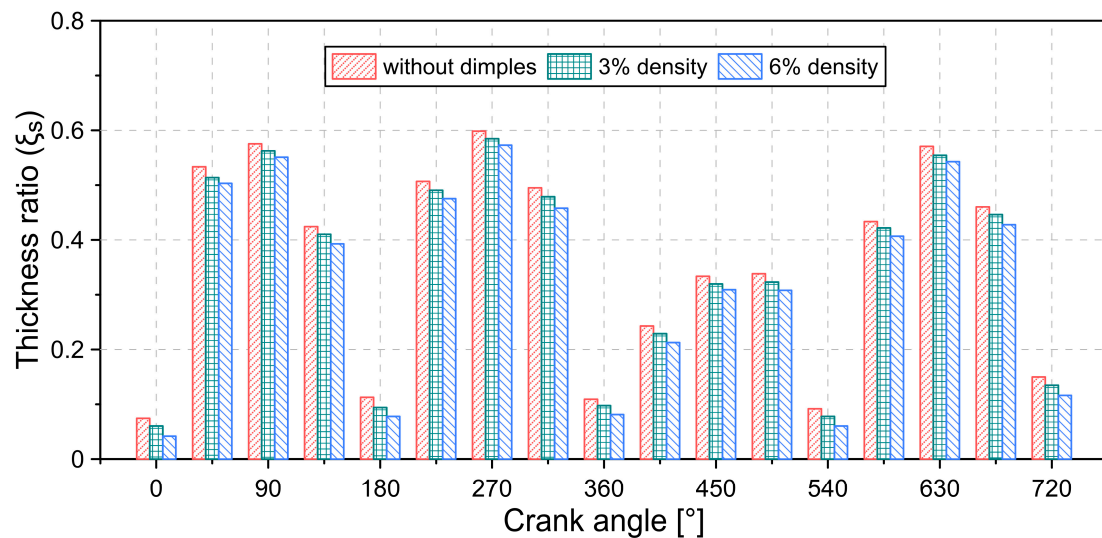The thickness ratio (ξ_s) throughout the combustion cycle is shown in Figure 11.

Figure 11. Thickness ratio for different dimple densities in flooded lubrication.

From the results of Figure 11, a decrease in the thickness ratio ζ_s was observed with the addition of dimples on the surface of the cylinder liner. This implies an increased risk of contact between the piston and the cylinder surface, especially during the engine's top dead center and bottom dead center, since, in these locations, the thinning of the lubricant film layer is greater. Therefore, the presence of dimples is a negative factor in flooded lubrication conditions.

The reduction in the lubricant film has a negative impact since the friction force increases, as shown in Figure 12. Overall, a 3.47% and 5.81% decrease in thickness was observed for a dimple density of 3% and 6%, respectively. From the results, an average thickness of 4.10 μm, 3.94 μm, and 3.82 μm was found throughout the combustion cycle for a cylinder liner without dimples, with 3% density and 6% density.
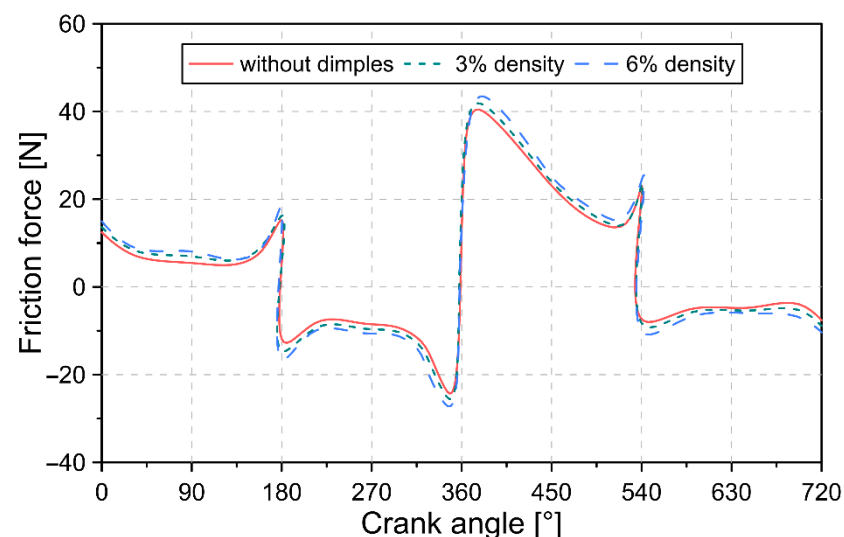

Figure 12. Friction force for different dimple densities in flooded lubrication.

The effect of dimple density under conditions of starved lubrication is shown in Figures 13 and 14.
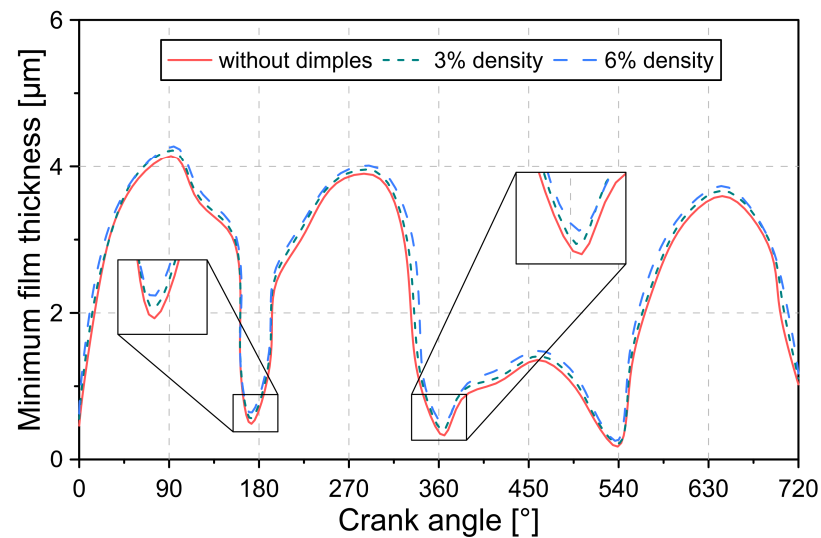
Figure 13. Minimum film thickness for different dimple densities in starved lubrication.
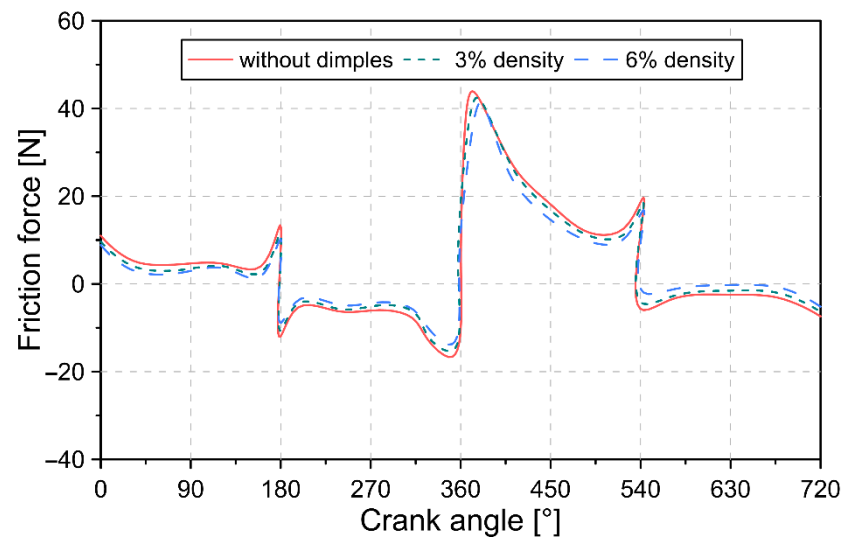

Figure 14. Friction force for different dimple densities in starved lubrication.

Figure 13 shows the behavior of the minimum film thickness under conditions of starved lubrication. From the results, it is evident that the increase in dimple density produces an increase in the thickness of the film, unlike the condition of flooded lubrication. Throughout the combustion cycle, the average minimum film thickness was 2.04 μm, 2.11 μm, and 2.19 μm for a no-dimples condition, 3% density, and 6% density in the cylinder liner, respectively. The increase in film thickness for the two densities evaluated was 6.06% and 12.60%. The effect of increasing film thickness on the friction force is shown in Figure 14.

In general, the results described in Figure 14 show that the increase in the thickness of the lubricant film produces a reduction in the frictional force. This is a consequence of the reduction in contacts due to the surface asperities between the face of the piston and the cylinder liner. Additionally, dimples in the cylinder liner under starved lubrication conditions allow oil storage, which helps to minimize dry rubbing and wet the contact interface. In general, a reduction in the friction force by 15.57% and 31.48% was revealed when establishing dimple densities of 3% and 6%, respectively.

Another geometric parameter considered for the evaluation of the effects of dimples on the cylinder liner on the tribological characteristics was the influence of the radius of the dimple (r_d) and the maximum depth of the dimple (h_d), which are described in Figure 15.
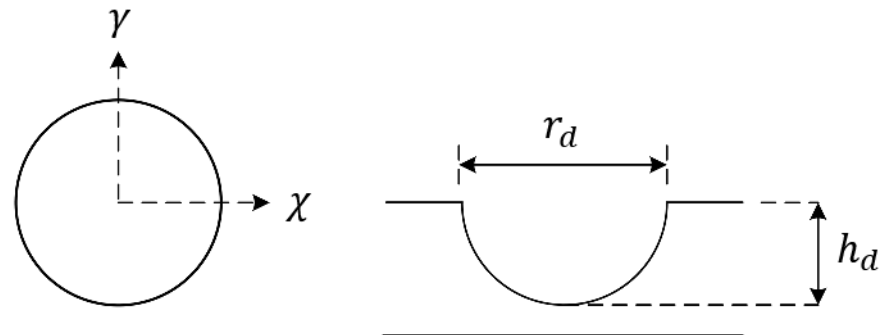

Figure 15. Geometry of the dimples on the cylinder liner.

Figure 16 shows the change in the minimum thickness of the lubricant film for different values of the radius of the dimple with a depth of 3 μm.
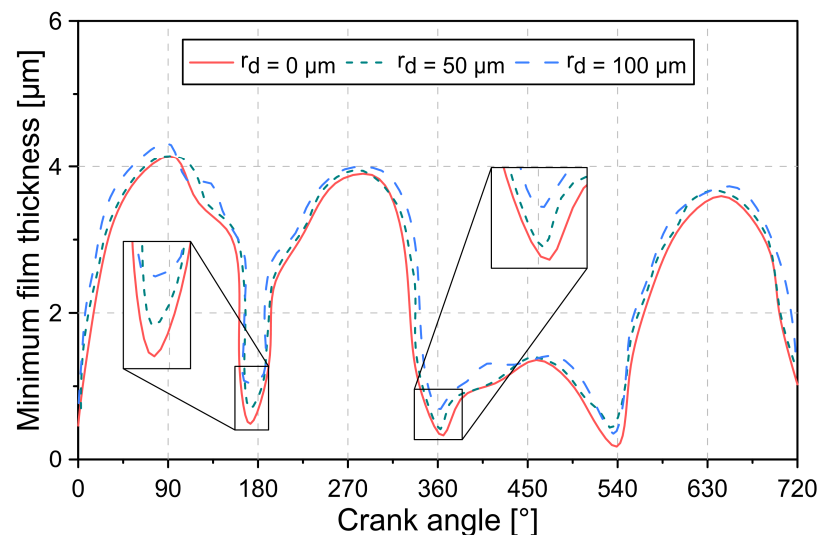

Figure 16. Minimum thickness of the lubricant film as a function of the radius of the dimple in starved lubrication.

From the results described in Figure 16, it was observed that the increase in the radius of the dimple produces an increase in the thickness of the lubrication film. This produces a decrease in the limit and viscous friction force supported by the piston rings. However, this behavior is especially evident for a dimple radius of 100 um. The maximum thickness of the lubricating oil film throughout the combustion cycle was 4.12 μm, 4.15 μm, and 4.31 μm for a dimple radius of 0 μm, 50 μm and 100 μm, respectively. Similar behavior was obtained by increasing the maximum depth of the dimple, as indicated in Figure 17.

Similar to the results of Figure 16, it was shown that the increase in the maximum depth of the dimple leads to an increase in the minimum thickness of the lubrication film. For the conditions evaluated, a maximum film thickness of 4.12 μm, 4.18 μm, and 4.26 μm was obtained for a maximum dimple depth of 0 μm, 2 μm, and 4 μm, respectively. In general, the results show that the dimple radius has a greater influence on the lubricant film thickness compared to the dimple depth.
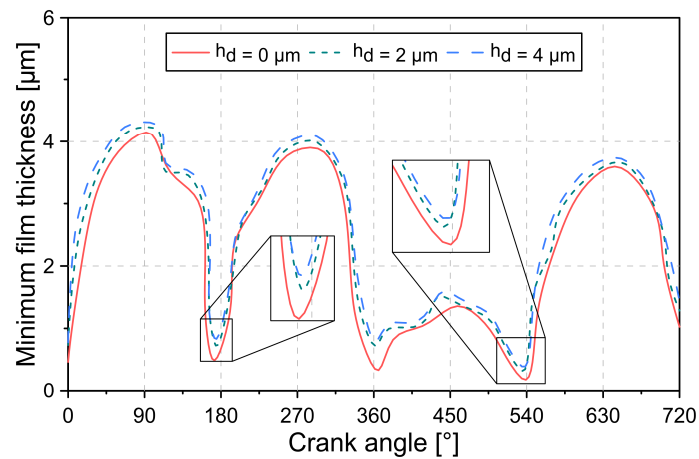
Figure 17. Minimum thickness of the lubricant film as a function of the maximum depth of the dimple and a constant radius of 75 µm in starved lubrication.

4.3. Influence of Geometric Dimple Distribution

To analyze the effect of the distribution of the dimples on the cylinder liner, three different designs are proposed, which are described in Figure 18. Each of the distributions presents the same geometric parameters in the dimples.
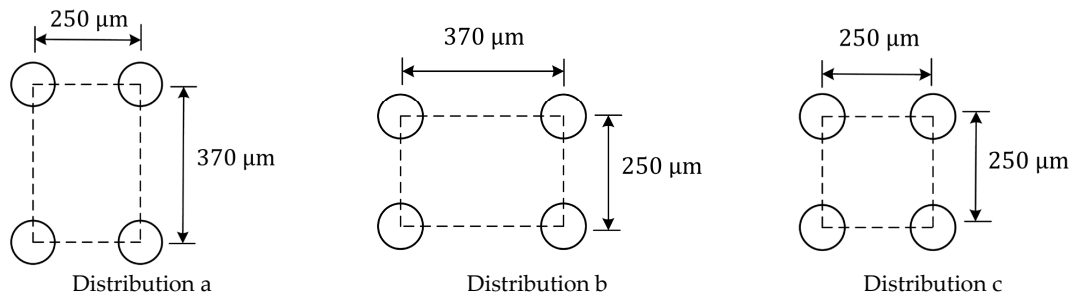

Figure 18. Type of dimple distributions in the cylinder liner ($r_d = 75$ µm , $h_d = 3$ µm).

Figure 19 shows the change in minimum lubricating oil film thickness for each crank angle in all three distributions.
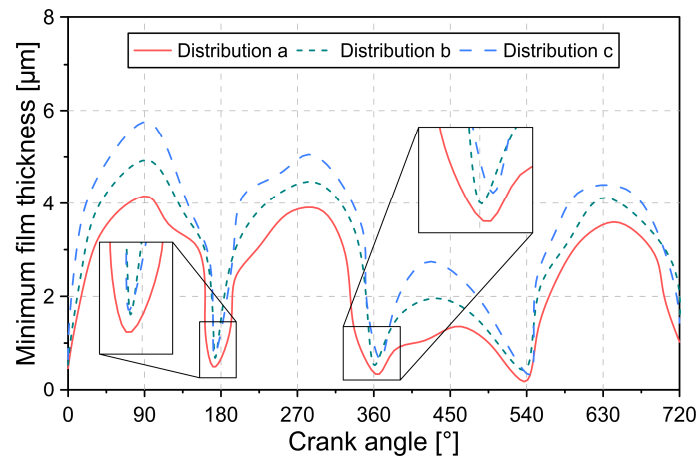

Figure 19. Minimum film thickness for different dimple distributions in starved lubrication.

From the results of Figure 19, it is evident that the trend of the minimum thickness of the film is maintained for each of the distributions. It was observed that the maximum thickness values occur at the middle position of the stroke, while the minimum values occur at the bottom dead center (BDC) and top dead center (TDC).

In general, the change in dimple distribution mainly affects the thickness at the middle position of the stroke. This can be attributed to the high sliding velocity of the piston rings at this position, which leads to an increase in the hydrodynamic effects generated by the presence of the dimples in the cylinder liner. However, the slip velocity is minimal during the BDC and TDC positions, and the hydrodynamic effects caused by the dimples on the cylinder liner are reduced. The maximum values in the lubricant film thickness were 4.15 μm, 4.93 μm, and 5.67 μm for distribution a, b and c, respectively.

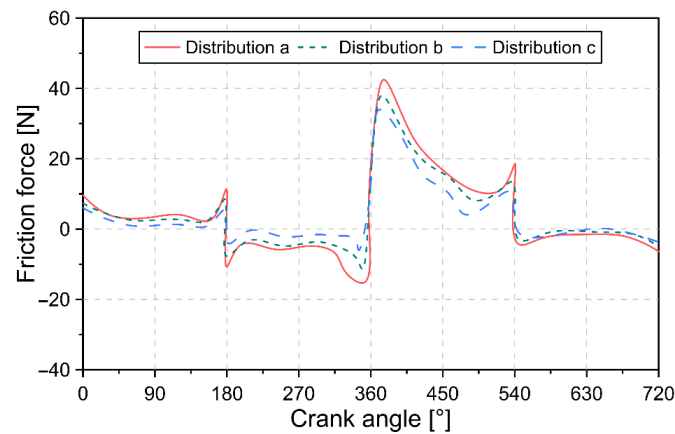Figure 20 shows the changes in the friction force for the different dimple distributions.

Figure 20. Friction force for different dimple distributions in starved lubrication.

In general, the magnitude of the friction force is relatively small at the intake and exhaust stages. This result is a consequence of the low-pressure loads inside the combustion chamber during these stages of the combustion cycle. Therefore, the contact of the surface asperities is limited. The above behavior is reversed during the compression and expansion stages of the piston due to the rapid increase in pressure. This causes a significant reduction in the thickness of the film and, therefore, an increase in the asperity force.

Additionally, the results indicate that the distribution of the dimples significantly impacts the friction force. In general, distribution c allowed a decrease of 24.98% and 10.53% in the maximum friction force, compared with distributions a and b, respectively. This implies a reduction in the net loss of power and the engine components' wear.

To evaluate the influence of dimple distributions on energy savings, a comparison of the power loss during the combustion cycle was made. The results obtained are shown in Figure 21.
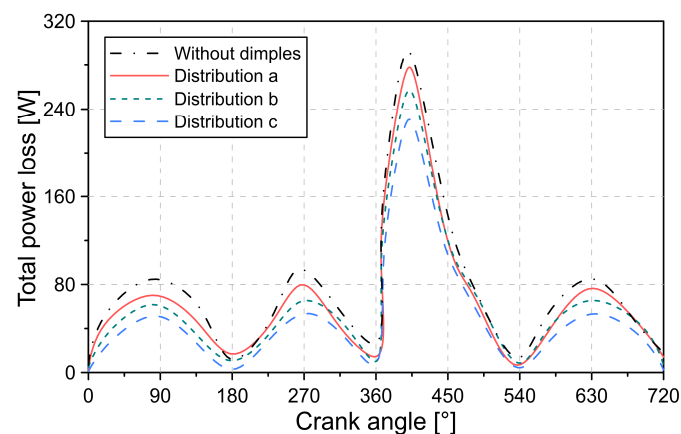

Figure 21. Total power loss for different dimple distributions in starved lubrication.

The results in Figure 21 indicate that the dimple distributions in the cylinder liner reduce the power loss throughout the combustion cycle. Distributions a, b, and c show a

5.2%, 12.3%, and 21.4% decrease in maximum power loss, compared with a surface without dimples.

4.4. Influence of the Geometric Parameters of the Honing Grooves

Figure 22 shows the effect of honing angle, honing groove density, and honing groove depth on the coefficient of friction.
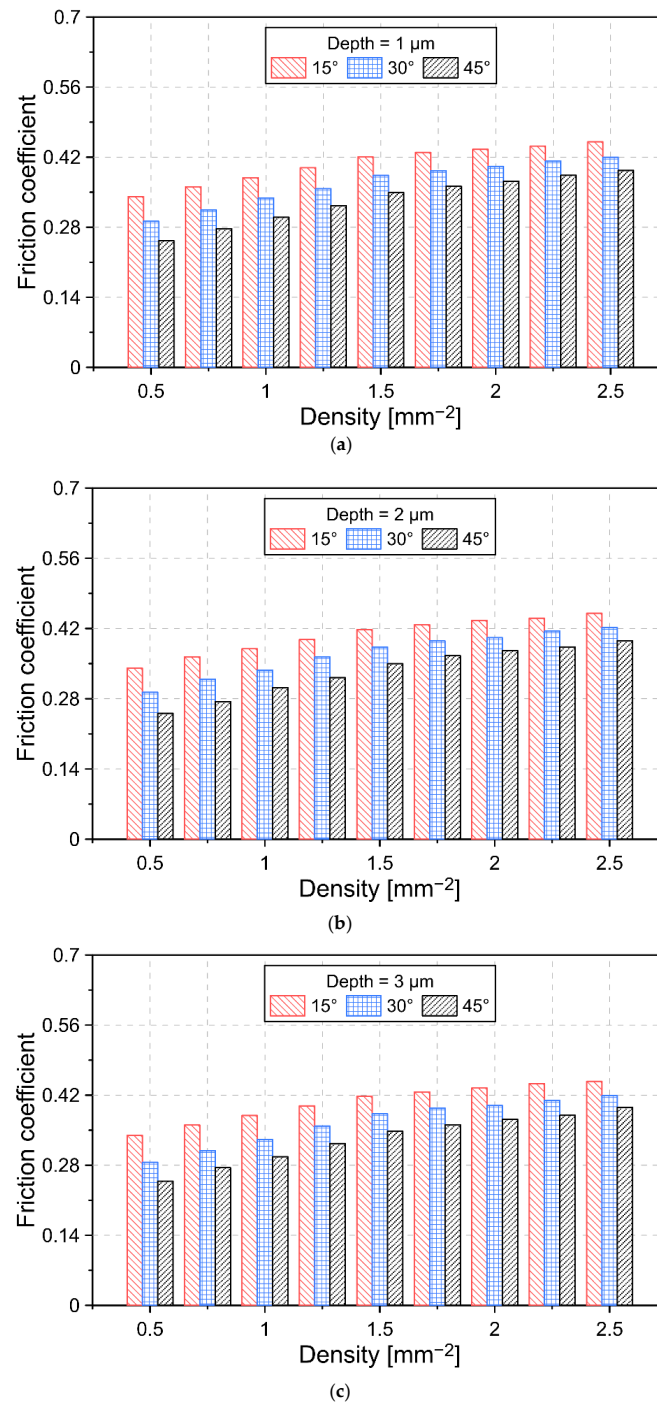

Figure 22. Influence of the honing grooves on the friction coefficient for a depth of (**a**) 1 μm, (**b**) 2 μm, and (**c**) 3 μm in starved lubrication.

According to the results of Figure 22, it is possible to show that the increase in the honing angle allows reducing the friction force. However, the increase in honing groove

density favors the increase in the coefficient of friction. The lowest coefficient of friction was obtained with a honing groove density of 0.5 mm^{-2}, which was 0.34, 0.29, and 0.25 for an angle of 15°, 30°, and 45°, respectively. In general, the effect of honing groove depth was not significant enough to cause a change in friction conditions.

To evaluate the influence of the honing grooves on the engine power loss, different types of textures with a depth of 3 μm and an inclination angle of 15°, 30°, and 45° were analyzed. The results obtained are shown in Figure 23.
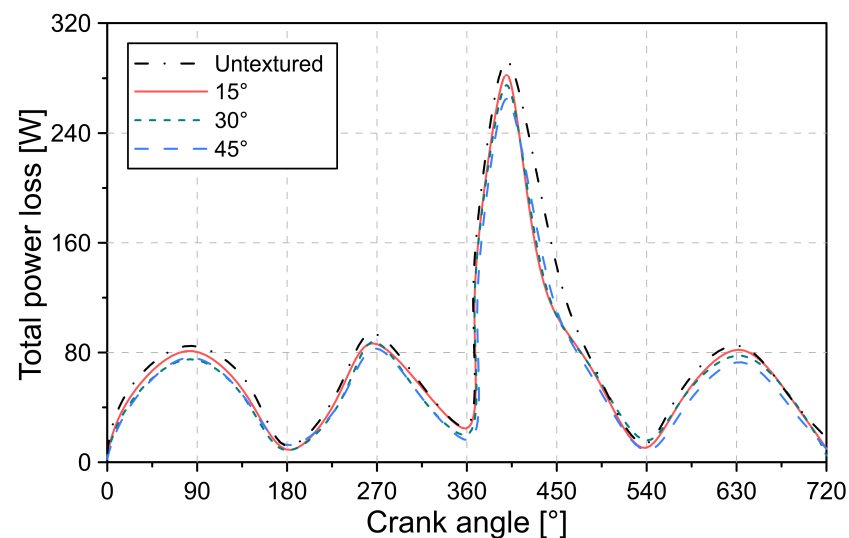

Figure 23. Total power loss for different honing grooves angles in starved lubrication.

In general, the results described in Figure 23 show that the honing groove texture allows for minimizing engine power losses. A 3.5%, 6.2%, and 9.6% decrease in power loss was obtained for the 15°, 30°, and 45° angled honing grooves, compared with an untextured surface.

5. Conclusions

In the present investigation, an analysis of the effects of dimples and honing grooves on the cylinder liner on the tribological characteristics of an internal combustion engine was carried out. For the study, a tribological model was used in order to determine the hydrodynamic behavior and the friction forces between the cylinder liner and piston. Additionally, the construction of a CFD model was carried out to describe the real dynamics of the piston. Numerical model validation was performed by comparing simulated results and experimental data. In general, a close similarity between the model predictions and the real behavior was obtained, obtaining an average relative error of 14%.

From the results, it was possible to conclude that the increase in dimple density has a positive impact on the increase in the lubricant film thickness and reduction in the friction force between the piston rings and the cylinder liner in starved lubrication conditions. In general, a 3% increase in dimple density led to a 3.79% increase in minimum lubrication film thickness and a 2.76% decrease in friction force. This allows reducing energy losses and wear of engine components. However, in flooded lubrication conditions, the presence of dimples in the cylinder liner does not allow a reduction in frictional force to be achieved. Despite the above, engines operate with starved lubrication during much of the combustion cycle.

The radius and depth of the dimple affect the tribological characteristics of the engine. The results show that the increase in the previous geometric parameters allows for increasing the minimum thickness of the lubrication film. In general, it was concluded that doubling the radius and depth of the dimple produced an increase of 3.86% and 1.91% in the minimum thickness of the lubrication film.

The most suitable distribution of the dimples on the surface of the cylinder liner corresponds to a square array (distribution c) since this allows a significant increase in the minimum thickness of the lubrication film, especially in the middle position of the piston stroke.

The analysis of the geometric parameters of the honing groove showed that the honing groove density and honing angle strongly influence the coefficient of friction. On average, a 15° increase in honing angle caused a 14.24% reduction in the coefficient of friction. However, excessively increasing honing groove density results in higher engine friction.

In general, the application of dimples and honing grooves in the cylinder liner are promising alternatives to reduce energy losses and minimize wear of engine components. Although both types of cylinder liner textures reduced power losses during the combustion cycle, a maximum decrease of 21.4% and 9.6% was observed with the dimples and honing grooves texture. However, it is necessary to build a regression model that allows finding the best geometric characteristics of both textures to demonstrate, which is the most appropriate. Future research will focus on this problem.

Abbreviations

The following abbreviations are used in this manuscript:

v_p	Piston velocity
h	Thickness of the lubrication film
P	Hydrodynamic pressure between the piston ring and the cylinder liner
T	Temperature
z	Lubricant piezo-viscosity index
s_o	Thermo-viscosity index
c_p, μ_∞	Model constants
h_m	Minimum film thickness
h_s	Profile of ring piston
h_p	Variation of the thickness of the lubricating oil film due to the dimples
h_h	Variation of the thickness of the lubricating oil film due to the honing groove
b	Piston ring axial width
r_d	Dimple radius
F_c	Experimental friction force
E_c	Young's modulus of the cylinder liner
h_d	Maximum depth of dimple
f_v	Viscous frictional force
f_b	Boundary frictional force
f_T	Total frictional force
v_{ss}	Viscous shear stress of lubricating oil
A	Apparent contact area
A_c	Real contact area between piston ring and cylinder liner
W_a	Asperity contact load
E'	Effective Young's modulus of elasticity

ν	Poisson's ratio
$F_{5/2}$, F_2	Statistical function
E	Young's modulus of elasticity
h_m	Minimum thickness of the lubrication film
l_{cl}	Clearance between the cylinder liner and the piston
Greek Letters	
ρ	Density of the lubricating oil
μ	Viscosity of the lubricating oil
ξ_s	Thickness ratio
ϕ_s	Shear flow factor
ϕ_x, ϕ_y	Pressure flow factors
ϕ_c	Contact factor
σ	Composite roughness
λ	Ratio of the thickness of the lubrication film
ϱ	Thermal coefficient of expansion
$\propto_o$	Viscosity coefficient (atmospheric piezo)
β_s	Viscosity coefficient (thermo)
δ_o	Crown height
χ, γ	Local cartesian coordinates for a single dimple cell
κ	Honing angle parameter
ω	Honing width parameter
ξ	Asperity distribution per unit contact area
φ	Average asperity tip radius of curvature
λ_s	Stribeck lubricant film ratio
ς	Coefficient of asperity shear strength
τ_o	Limiting Eyring shear stress

References

1. Gurt, A.; Khonsari, M. The Use of Entropy in Modeling the Mechanical Degradation of Grease. *Lubricants* **2019**, *7*, 82. [CrossRef]
2. Chong, W.W.F.; Hamdan, S.H.; Wong, K.J.; Yusup, S. Modelling Transitions in Regimes of Lubrication for Rough Surface Contact. *Lubricants* **2019**, *7*, 77. [CrossRef]
3. Tung, S.C.; McMillan, M.L. Automotive Tribology Overview of Current Advances and Challenges for the Future. *Tribol. Int.* **2004**, *37*, 517–536. [CrossRef]
4. Holmberg, K.; Andersson, P.; Erdemir, A. Global Energy Consumption Due to Friction in Passenger Cars. *Tribol. Int.* **2012**, *47*, 221–234. [CrossRef]
5. Söderfjäll, M.; Herbst, H.M.; Larsson, R.; Almqvist, A. Influence on Friction from Piston Ring Design, Cylinder Liner Roughness and Lubricant Properties. *Tribol. Int.* **2017**, *116*, 272–284. [CrossRef]
6. Rahmani, R.; Rahnejat, H.; Fitzsimons, B.; Dowson, D. The Effect of Cylinder Liner Operating Temperature on Frictional Loss and Engine Emissions in Piston Ring Conjunction. *Appl. Energy* **2017**, *191*, 568–581. [CrossRef]
7. Furuhama, S.; Sumi, T. A Dynamic Theory of Piston-Ring Lubrication: 3rd Report, Measurement of Oil Film Thickness. *Bull. JSME* **1961**, *4*, 744–752. [CrossRef]
8. Ma, M.-T.; Sherrington, I.; Smith, E.H. Analysis of Lubrication and Friction for a Complete Piston-Ring Pack with an Improved Oil Availability Model: Part 1: Circumferentially Uniform Film. *Proc. Inst. Mech. Eng. Part J J. Eng. Tribol.* **1997**, *211*, 1–15. [CrossRef]
9. Akalin, O.; Newaz, G.M. Piston Ring-Cylinder Bore Friction Modeling in Mixed Lubrication Regime: Part I—Analytical Results. *J. Trib.* **2001**, *123*, 211–218. [CrossRef]
10. Jeng, Y.-R. Theoretical Analysis of Piston-Ring Lubrication Part II—Starved Lubrication and Its Application to a Complete Ring Pack. *Tribol. Trans.* **1992**, *35*, 707–714. [CrossRef]
11. Furuhama, S.; Sasaki, S. New Device for the Measurement of Piston Frictional Forces in Small Engines. *SAE Trans.* **1983**, *92*, 781–792.
12. Tian, T. Dynamic Behaviours of Piston Rings and Their Practical Impact. Part 2: Oil Transport, Friction and Wear of Ring/Liner Interface and the Effects of Piston and Ring Dynamics. *Proc. Inst. Mech. Eng. Part J J. Eng. Tribol.* **2002**, *216*, 229–248. [CrossRef]
13. Morris, N.; Mohammadpour, M.; Rahmani, R.; Rahnejat, H. Optimisation of the Piston Compression Ring for Improved Energy Efficiency of High Performance Race Engines. *Proc. Inst. Mech. Eng. Part D J. Automob. Eng.* **2017**, *231*, 1806–1817. [CrossRef]
14. Bewsher, S.R.; Leighton, M.; Mohammadpour, M.; Rahnejat, H.; Offner, G.; Knaus, O. Atomic Force Microscopic Measurement of a Used Cylinder Liner for Prediction of Boundary Friction. *Proc. Inst. Mech. Eng. Part. D J. Automob. Eng.* **2019**, *233*, 1879–1889. [CrossRef]
15. Usman, A.; Park, C.W. Modeling and Simulation of Frictional Energy Loss in Mixed Lubrication of a Textured Piston Compression Ring during Warm-up of Spark Ignition Engine. *Int. J. Engine Res.* **2017**, *18*, 293–307. [CrossRef]

16. Howell-Smith, S.; Rahnejat, H.; King, P.D.; Dowson, D. Reducing In-Cylinder Parasitic Losses through Surface Modification and Coating. *Proc. Inst. Mech. Eng. Part D J. Automob. Eng.* **2014**, *228*, 391–402. [CrossRef]
17. Li, C.-D.; Jin, M.; Du, F.-M.; Wang, W.-W.; Shen, Y.; Xu, J.-J. Wear Behavior of Al-Si Alloy Cylinder Liner Prepared by Laser Finishing. *Proc. Inst. Mech. Eng. Part D J. Automob. Eng.* **2018**, *232*, 1944–1949. [CrossRef]
18. Senatore, A.; Risitano, G.; Scappaticci, L.; D'Andrea, D. Investigation of the Tribological Properties of Different Textured Lead Bronze Coatings under Severe Load Conditions. *Lubricants* **2021**, *9*, 34. [CrossRef]
19. Shum, P.W.; Zhou, Z.F.; Li, K.Y. Investigation of the Tribological Properties of the Different Textured DLC Coatings under Reciprocating Lubricated Conditions. *Tribol. Int.* **2013**, *65*, 259–264. [CrossRef]
20. Wang, X.; Liu, W.; Zhou, F.; Zhu, D. Preliminary Investigation of the Effect of Dimple Size on Friction in Line Contacts. *Tribol. Int.* **2009**, *42*, 1118–1123. [CrossRef]
21. Kligerman, Y.; Etsion, I.; Shinkarenko, A. Improving Tribological Performance of Piston Rings by Partial Surface Texturing. *J. Trib.* **2005**, *127*, 632–638. [CrossRef]
22. Spencer, A. Optimizing Surface Texture for Combustion Engine Cylinder Liners. Ph.D. Thesis, Luleåtekniska Universitet, Luleå, Sweden, 2010.
23. Lu, P.; Wood, R.J.K. Tribological Performance of Surface Texturing in Mechanical Applications—A Review. *Surf. Topogr. Metrol. Prop.* **2020**, *8*, 43001. [CrossRef]
24. Etsion, I. Surface Texturing for In-Cylinder Friction Reduction. *Tribol. Dyn. Engine Powertrain* **2010**, 458–470. [CrossRef]
25. Paranjpe, R.S.; Cusenza, A. FLARE: An Integrated Software Package for Friction and Lubrication Analysis of Automotive Engines-Part II: Experimental Validation. *SAE Tech. Pap.* **1992**, 920488. [CrossRef]
26. Hu, Y.; Meng, X.; Xie, Y. A New Efficient Flow Continuity Lubrication Model for the Piston Ring-Pack with Consideration of Oil Storage of the Cross-Hatched Texture. *Tribol. Int.* **2018**, *119*, 443–463. [CrossRef]
27. Vladescu, S.-C.; Medina, S.; Olver, A.V.; Pegg, I.G.; Reddyhoff, T. Lubricant Film Thickness and Friction Force Measurements in a Laser Surface Textured Reciprocating Line Contact Simulating the Piston Ring–Liner Pairing. *Tribol. Int.* **2016**, *98*, 317–329. [CrossRef]
28. Pawlus, P.; Dzierwa, A.; Michalski, J.; Reizer, R.; Wieczorowski, M.; Majchrowski, R. The Effect of Selected Parameters of the Honing Process on Cylinder Liner Surface Topography. *Surf. Topogr. Metrol. Prop.* **2014**, *2*, 25004. [CrossRef]
29. Jeng, Y.-R. Impact of Plateaued Surfaces on Tribological Performance. *Tribol. Trans.* **1996**, *39*, 354–361. [CrossRef]
30. Vlădescu, S.-C.; Ciniero, A.; Tufail, K.; Gangopadhyay, A.; Reddyhoff, T. Looking into a Laser Textured Piston Ring-Liner Contact. *Tribol. Int.* **2017**, *115*, 140–153. [CrossRef]
31. Guo, Y.; Lu, X.; Li, W.; He, T.; Zou, D. A Mixed-Lubrication Model Considering Elastoplastic Contact for a Piston Ring and Application to a Ring Pack. *Proc. Inst. Mech. Eng. Part D J. Automob. Eng.* **2015**, *229*, 174–188. [CrossRef]
32. Patir, N.; Cheng, H.S. An Average Flow Model for Determining Effects of Three-Dimensional Roughness on Partial Hydrodynamic Lubrication. *J. Lubricants Technol.* **1978**, *100*, 12–17. [CrossRef]
33. Dowson, D.; Higginson, G.R. A Numerical Solution to the Elasto-Hydrodynamic Problem. *J. Mech. Eng. Sci.* **1959**, *1*, 6–15. [CrossRef]
34. Houpert, L. New Results of Traction Force Calculations in Elastohydrodynamic Contacts. *J. Tribol.* **1985**, *107*, 241–245. [CrossRef]
35. Gu, C.; Meng, X.; Xie, Y.; Kong, X. Performance of Surface Texturing during Start-up under Starved and Mixed Lubrication. *J. Tribol.* **2017**, *139*, 11702. [CrossRef]
36. Ronen, A.; Etsion, I.; Kligerman, Y. Friction-Reducing Surface-Texturing in Reciprocating Automotive Components. *Tribol. Trans.* **2001**, *44*, 359–366. [CrossRef]
37. Spencer, A.; Almqvist, A.; Larsson, R. A Semi-Deterministic Texture-Roughness Model of the Piston Ring–Cylinder Liner Contact. *Proc. Inst. Mech. Eng. Part J J. Eng. Tribol.* **2011**, *225*, 325–333. [CrossRef]
38. Rahmani, R.; Theodossiades, S.; Rahnejat, H.; Fitzsimons, B. Transient Elastohydrodynamic Lubrication of Rough New or Worn Piston Compression Ring Conjunction with an Out-of-Round Cylinder Bore. *Proc. Inst. Mech. Eng. Part J J. Eng. Tribol.* **2012**, *226*, 284–305. [CrossRef]
39. Zavos, A.; Nikolakopoulos, P.G. Investigation of the Top Compression Ring Power Loss and Energy Consumption for Different Engine Conditions. *Tribol. Surfaces Interfaces* **2021**, *1*, 1–13. [CrossRef]
40. Greenwood, J.A.; Tripp, J.H. The Contact of Two Nominally Flat Rough Surfaces. *Proc. Inst. Mech. Eng.* **1970**, *185*, 625–633. [CrossRef]
41. Teodorescu, M.; Balakrishnan, S.; Rahnejat, H. Integrated Tribological Analysis within a Multi- Physics Approach to System Dynamics. *Tribol. Interface Eng. Ser.* **2005**, *48*, 725–737.
42. Popoola, O.; Cao, Y. The Influence of Turbulence Models on the Accuracy of CFD Analysis of a Reciprocating Mechanism Driven Heat Loop. *Case Stud. Therm. Eng.* **2016**, *8*, 277–290. [CrossRef]
43. Koch, F.; Decker, P.; Gülpen, R.; Quadflieg, F.J.; Loeprecht, M. Cylinder Liner Deformation Analysis—Measurements and Calculations. *SAE Trans.* **1998**, *107*, 838–847.
44. Zavos, A.; Nikolakopoulos, P.G. Tribology of New Thin Compression Ring of Fired Engine under Controlled Conditions-A Combined Experimental and Numerical Study. *Tribol. Int.* **2018**, *128*, 214–230. [CrossRef]
45. Tsujiuchi, N.; Koizumi, T.; Hamada, K.; Okamura, M.; Tsukijima, H. Optimization of Profile for Reduction of Piston Slap Excitation. In Proceedings of the Small Engine Technology Conference & Exposition, Graz, Austria, 27–30 September 2004; SAE: Warrendale, PA, USA, 2004.
46. Gore, M.; Theaker, M.; Howell-Smith, S.; Rahnejat, H.; King, P.D. Direct Measurement of Piston Friction of Internal-Combustion Engines Using the Floating-Liner Principle. *Proc. Inst. Mech. Eng. Part D J. Automob. Eng.* **2014**, *228*, 344–354. [CrossRef]